The Astronomical Journal, 164:230 (12pp), 2022 December https://doi.org/10.3847/1538-3881/ac8df0

The Arizona Radio Observatory 1 mm Spectral Survey of the Hypergiant Star NML Cygni (215–285 GHz)

A. P. Singh[1], J. L. Edwards[1], and L. M. Ziurys[1,2]
[1] Department of Chemistry, The University of Arizona PO Box 210041, Tucson, AZ 85721 USA; lziurys@email.arizona.edu
[2] Department of Astronomy and Steward Observatory, Arizona Radio Observatory, The University of Arizona 933 North Cherry Avenue, Tucson, AZ 85721 USA
Received 2022 March 26; revised 2022 August 11; accepted 2022 August 29; published 2022 November 1

Abstract

A sensitive (1σ rms $\leqslant 3$ mK; 2 MHz resolution) 1 mm spectral survey (214.5–285.5 GHz) of the envelope of the oxygen-rich supergiant star NML Cygni (NML Cyg) has been conducted using the 10 m Submillimeter Telescope of the Arizona Radio Observatory. These data represent the first spectral line survey of NML Cyg and are complementary to a previous 1 mm survey of the envelope of a similar hypergiant, VY Canis Majoris (VY CMa). The complete NML Cyg data set is presented here. In the survey, 104 emission lines were observed, arising from 17 different molecules and 4 unidentified features. Many of the observed features have complex line profiles, arising from asymmetric outflows characteristic of hypergiant stars. While most of the lines in the survey arise from SiO, SO, SO_2, and SiS, CO had the strongest emission. Five other C-bearing species are identified in the survey (HCN, CN, HCO^+, CS, and HNC), demonstrating an active carbon chemistry despite the O-rich environment. Moreover, NS was observed, but not NO, although favorable transitions of both molecules lie in the surveyed region. Sulfur chemistry appears to be prominent in NML Cyg and plays an important role in the collimated outflows. The refractory species observed, NaCl and AlO, have narrow emission lines, indicating that these molecules do not reach the terminal expansion velocity. NaCl and AlO likely condense into dust grains at $r < 50\ R_*$. From NaCl, the chlorine isotope ratio was determined to be $^{35}Cl/^{37}Cl = 3.85 \pm 0.30$.

Unified Astronomy Thesaurus concepts: Circumstellar envelopes (237); Hypergiant stars (774); Millimeter astronomy (1061); Molecular spectroscopy (2095); Astrochemistry (75); Stellar mass loss (1613); Stellar winds (1636); Stellar evolution (1599); Isotopic abundances (867)

Supporting material: extended figure

1. Introduction

CO is thought to be the prominent carrier of the gas-phase carbon in the envelopes of oxygen-rich stars (e.g., Höfner & Olofsson 2018). Therefore, it was believed for decades that such envelopes would have a simplistic chemistry, dominated by SiO, H_2O, and OH (Nercessian et al. 1989; Olofsson 2005). Early observations, however, hinted a greater chemical complexity, as some O-rich shells contained other carbon-bearing species, such as HCN, CN, and CS (e.g., Deguchi & Goldsmith 1985; Olofsson et al. 1991), and were apparently rich in sulfur-containing molecules, including SO, SO_2, and H_2S (Omont et al. 1993). The work of Tenenbaum et al. (2010a, 2010b) finally showed that O-rich envelopes have a unique and interesting chemistry, as proven through a sensitive (1σ rms $\sim$3 mK) 1 mm spectral line survey of the hypergiant star VY Canis Majoris (VY CMa), conducted with the Submillimeter Telescope (SMT) of the Arizona Radio Observatory (ARO). Not only were a number of new molecules discovered in the envelope of VY CMa (PO, AlOH, AlO, and later TiO, TiO_2, and VO; see Tenenbaum et al. 2007; Tenenbaum & Ziurys 2009, 2010; Kamiński et al. 2013; Humphreys et al. 2019), but unusual molecular line profiles were observed, with sharp blue- and redshifted peaks, showcasing the nonisotropic outflows associated with this active star. Subsequently, the envelope of the asymptotic giant branch (AGB) star IK Tauri (IK Tau) was extensively studied through another spectral line survey, demonstrating that it too has a complex chemical environment (Velilla Prieto et al. 2017).

Oxygen-rich circumstellar envelopes are common, as $O > C$ in the general interstellar medium. Stars on the early-AGB (E-AGB), as well as supergiants, are O-rich, and some have substantial mass-loss rates and extensive envelopes. It is not until the thermal-pulsing (TP) phase on the latter part of the AGB that third dredge-up (TDU) mixes carbon from the helium-burning shell to the stellar photosphere, eventually tipping the C/O ratio in favor of carbon (Herwig 2000). Therefore, it is important to understand the chemical makeup of O-rich shells, as well as C-rich ones.

Hypergiant stars like VY CMa have also been objects of interest due to their high mass-loss rates and complex, sporadic ejection events. Such mass loss creates a large, dynamic circumstellar envelope (Humphreys et al. 2021), with outflows that are highly collimated, unlike the largely spherically symmetric shells of AGB stars. For example, nonisotropic outflows are clearly present in the envelope of VY CMa, as demonstrated by the Hubble Space Telescope and other images in the infrared (e.g., Humphreys et al. 2007, 2019, 2021). These asymmetric winds are also apparent in molecular spectral lines, as mentioned, and are found to have their own peculiar chemistry, traced best by sulfur-bearing species such as SO and SO_2 (e,g. Ziurys et al. 2007; Tenenbaum et al. 2010a, 2010b; Adande et al. 2013). The outflows are evident in nonsymmetrical red- and blueshifted velocity components, superimposed over what appears to be a spherical wind at the star's systemic velocity.

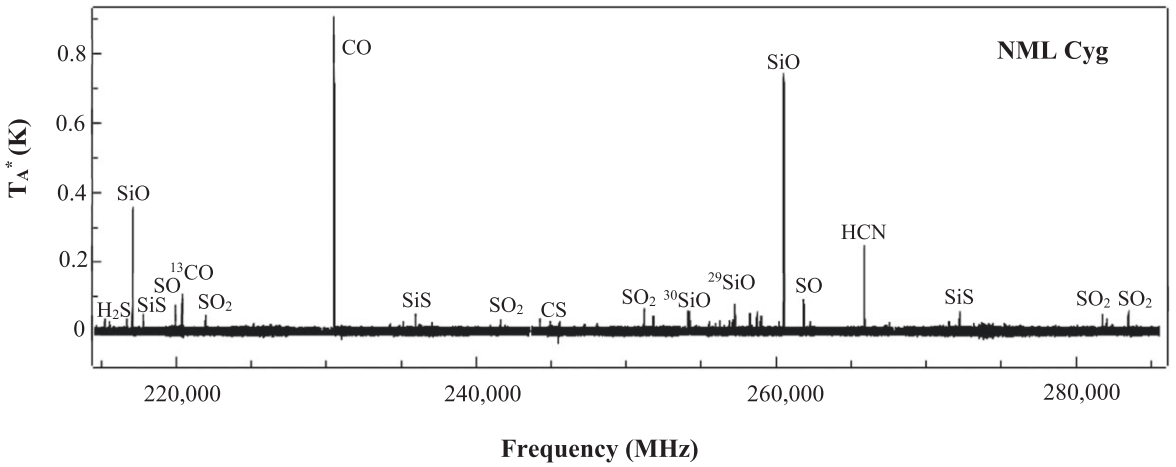

Figure 1. The composite 1 mm survey of NML Cyg covering the frequency range 214.5–285.5, plotted on a temperature scale (T_A^*) set by the strongest feature, CO, $J = 2 \rightarrow 1$. Also prominent in the spectrum is HCN and SiO, while SO, SO_2, and SiS have weaker emission.

Another hypergiant of note is NML Cygnus, or NML Cyg. Like VY CMa, NML Cyg has a high mass-loss rate of $\sim 10^{-4}$ $M_\odot$ (Netzer & Knapp 1987; Etoka & Diamond 2004), and exhibits a dusty circumstellar envelope that contains a bean-shaped structure (Schuster et al. 2006, 2009). The envelope is thought to be influenced by the hot stars of the nearby Cyg OB2 association, although the extent of this interaction is debated (e.g., Schuster et al. 2009; Zhang et al. 2012a). Much of the past work on NML Cyg has focused on maser emission from OH, H_2O, and SiO (e.g., Cohen et al. 1987; Richards et al. 1996; Boboltz & Claussen 2004; Nagayama et al. 2008). Other molecules subsequently have been identified in NML Cyg, including CO, CO_2, HCN, SO, SO_2, H_2S, NH_3, and HCO^+ (e.g., Justtanont et al. 1996; Nercessian et al. 1989; Omont et al. 1993; Ziurys et al. 2009; Pulliam et al. 2011; Teyssier et al. 2012). This source has recently become the object of spectral line surveys, as well. First, as reported here, a sensitive (1σ rms $\leqslant$ 3 mK, 2 MHz resolution) 1 mm survey (214.5–285.5 GHz) was conducted of NML Cyg, using the ARO SMT, in analogy to that carried out for VY CMa by Tenenbaum et al. (2010a, 2010b). The highlights of this survey have already been published (Singh et al. 2021). The most striking result of this work is that the chemical composition of the envelope closely resembles that of VY CMa, with the detection of the same carbon- and sulfur-bearing species, but also the more exotic molecules NaCl, AlO, PO, and PN (also see Ziurys et al. 2018). Furthermore, the line profiles of certain molecules such as SO_2 and SO show evidence of asymmetric outflows, with a blueshifted component near $V_{\rm LSR} = -21 \pm 3$ km s^{-1} and a collimated, redshifted component near 15 ± 3 km s^{-1}. Similar asymmetric winds were found for VY CMa, making NML Cyg a close "twin." Andrews et al. (2022) also have conducted a 68–116 GHz spectral survey of the envelope of NML Cyg, using the Onsala 20 m telescope. They observed fewer molecules than in the ARO 1 mm survey (CO, SO, SO_2, HCN, SiO, and SiS), but modeled multiple CO and SiO lines from other measurements (Herschel Space Observatory, James Clerk Maxwell Telescope). They also concluded there were multiple collimated outflows in the envelope of NML Cyg.

The initial paper on the ARO SMT 1 mm survey of NML Cyg concerned only a small fraction of the observed spectra and focused on the physical structure of the outflows. In this work, the complete survey is presented, including line assignments and measured parameters for all spectral features. An interpretation of the chemistry and spatial distributions of the molecules is given, as well as carbon, sulfur, oxygen, chlorine, and silicon isotope ratios.

2. Observations

The measurements were conducted between 2008 March and 2014 March using the ARO 10 m SMT on Mt. Graham, Arizona. The dual polarization 1 mm receiver was equipped with ALMA Band 6 sideband separating (SBS) superconductor-insulator-superconductor mixers. Image rejection was typically $\geqslant$16 dB, intrinsic in the mixer architecture. The backend used was a 2048-channel, 1 MHz resolution filter bank, configured in parallel mode (2×1024 channels) to accommodate both receiver polarizations. The temperature scale at the SMT is T_A^*, determined by the chopper wheel method, where $T_R = T_A^*/\eta_b$. Here T_R is the main beam brightness temperature, and η_b is the beam efficiency. The average beam efficiency over the 1 mm band (215 GHz–285 GHz) was $\eta_b = 0.74$–0.70 with the beam size ranging from $\theta_b = 35''$–$26''$. The spectra were measured in 1 GHz intervals, as dictated by the instantaneous bandwidth of the backend (1.024 GHz), allowing for some overlap between settings, over the range of 214.5–285.5 GHz. The data were typically observed in the lower sideband (LSB) for frequencies below 230 GHz, and upper sideband (USB) above that frequency. However, sidebands were also chosen to avoid image contamination, as was the receiver intermediate frequency, varied between 5–7 GHz. Local oscillator shifts of $\pm$20 MHz were also done at all frequencies to test for image contamination.

Observations were conducted in beam-switching mode with a subreflector throw of $\pm 2'$ toward $\alpha = 20^{\rm h}44^{\rm m}33\overset{\rm s}{.}8$, $\delta = 39°\,55'57\overset{''}{.}0$ (B1950.0), using $V_{\rm LSR} = -1$ km s^{-1}, the systemic velocity of the source (Kemper et al. 2003; Etoka & Diamond 2004). Pointing and focus were checked on planets or strong continuum sources every 1–2 hr. Each frequency setting was observed until at least a 1σ rms of $\sim$3 mK was achieved (2 MHz resolution). Line identification was performed using the detection limit of 5σ rms. Approximately 800 hr of actual integration time were required for the survey (about 12 hr per 1 GHz frequency interval), not including overhead, pointing, and receiver tuning. Strong lines in the survey such as

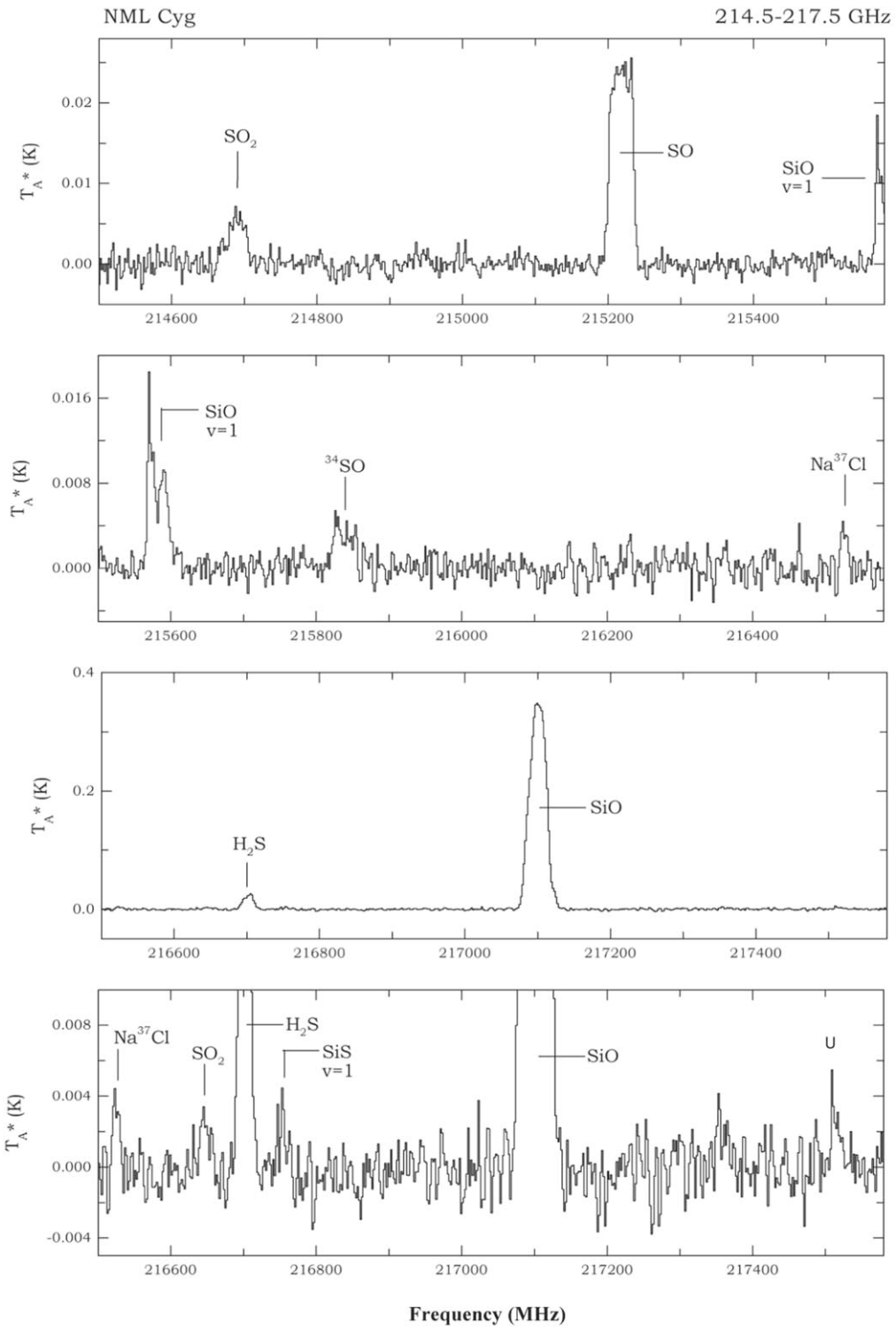

Figure 2. The 1 mm survey (214.5–285.5 GHz) of NML Cyg displayed in consecutive ∼1 GHz frequency segments. Temperature scale in T_A^*(K) and spectral resolution is 2 MHz. There is 40–80 MHz overlap between consecutive spectra in order to show any lines on the edge of a given range for display purposes. For frequencies with lines stronger than $T_A^* \sim 50$ mK, a second version of the spectrum is shown with a more sensitive scale. Each emission feature is marked with its molecular identification. First order baselines were removed from each spectrum. Integration time per spectrum is typically ∼15 hr.

(An extended version of this figure is available.)

those of CO, SiO (v = 0), and SiS were routinely measured for calibration purposes. Variations in line intensities were not observed. Data were reduced using UNIPOPS software package (Astrophysical Source Code Library, ascl 1503.007), and linear baselines were removed.

3. Results and Analysis

Figure 1 provides a snapshot of the entire survey with the intensity scale determined by the strongest feature, CO: $J = 2 \rightarrow 1$, which has an antenna temperature of $T_A^* \sim 0.9$ K. Note that Galactic contamination was removed from the CO

Table 1
Molecular Lines Observed in the 1 mm Spectrum of NML Cyg

Molecule	Variations	No. of Lines
CO	^{13}CO	2
SiO	v = 1, v = 2, ^{29}SiO, ^{30}SiO, Si^{18}O	9
SiS	v = 1, ^{29}SiS, ^{30}SiS, Si^{34}S	17
SO	^{34}SO	8
CS		1
CN		2
NS		2
NaCl	v = 1, Na^{37}Cl	13
PN		2
PO		4
AlO		1
H_2O	$v_2 = 2$	1
H_2S		1
HCN	$v_2 = 1$, H^{13}CN	3
HNC		1
SO_2	$^{34}SO_2$,SO^{18}O	32
HCO^+		1
U		4
	Total Number of Lines	104

line profile in the figure (see Figure 2). Aside from CO, HCN and SiO (v = 0) have the most intense emission features, as well as ^{13}CO and ^{29}SiO. Many lines of SO, SO_2, and SiS are also apparent. The lines which are prominent in the 1 mm spectrum of VY CMa, maser lines arising from $v_2 = 1$ state of H_2O and the v = 2 state of ^{29}SiO, are either much weaker or not detected. Both these features appear to be time variable in VY CMa, however, and may be stronger at another epoch in NML Cyg. In general, the emission lines in NML Cyg are about a factor of 2 weaker than in VY CMa, easily attributed to its greater distance (1.6 versus 1.1 kpc: see Singh et al. 2021).

The complete 1 mm survey of NML Cyg, presented in ~1 GHz frequency intervals, as per the observations, is shown in Figure 2. The first and final panels are centered near 215.0 and 285.0 GHz, respectively. The intensity scale is T_A^* (K), and the spectral resolution is 2 MHz, smoothed from 1 MHz. There is overlap of ~80–100 MHz at the higher frequency end of each spectral interval in order to accommodate broad lines near the bandpass edge, for presentation purposes. For example, the first panel shows the frequency range 214.500–215.580 MHz. If there are strong lines in a given frequency interval, a second spectrum showing the weaker features is displayed below the full-scale data. Molecular identifications are shown on the spectra, based on the catalogs of Jet Propulsion Laboratory (JPL; Pickett et al. 1998), and Cologne Database for Molecular Spectroscopy (CDMS; Müller et al. 2005). For transitions not occurring in the ground state, the vibrational quantum number is shown. Unidentified features are labeled "U." In order to positively identify a given line, all corresponding feasible molecular transitions had to be present at reasonable intensity levels.

Overall, 104 emission features from 17 different molecules, as well as 4 unidentified lines, were identified in the circumstellar envelope of NML Cyg. Common species such as CO, CS, SiO, SiS, SO, SO_2, H_2S, H_2O, HCN, HNC, HCO^+, and CN are present in the survey, along with the more exotic species AlO, NaCl, NS, PN, and PO. A number of isotopologues were also identified: ^{13}CO, H^{13}CN, ^{29}SiS, ^{30}SiS, Si^{34}S, ^{29}SiO, ^{30}SiO, Si^{18}O, ^{34}SO, $^{34}SO_2$, SO^{18}O, and Na^{37}Cl. Lines arising from vibrationally excited states include NaCl (v = 1), SiS (v = 1), and SiO (v = 1 and 2), HCN ($v_2 = 1$), and H_2O ($v_2 = 2$). A summary of the molecules and their observed transitions is given in Table 1, including isotopic variants and vibrationally excited levels. Note that the one identified HCO^+ transition in the survey ($J = 3 \rightarrow 2$), is blended with SO_2; confirming lines were observed by Pulliam et al. (2011).

Table 2 lists the observed spectral features from the survey and their measured line parameters, as well as the rest frequencies and assigned transitions. Unidentified features are assigned a frequency based on $V_{LSR} = -1$ km s^{-1}, an average value based on other works (Kemper et al. 2003; Etoka & Diamond 2004). The line parameters for almost all spectral features were determined by fits to the profiles using the non–local thermodynamic equilibrium radiative transfer code, ESCAPADE (Adande et al. 2013). This code employs the escape probability formalism to decouple the radiative transfer from the calculations of the level populations, assuming uniform expansion velocity, within the Sobolev approximation, and can be used to model spherically symmetric or directional (asymmetric) conical outflows (also see Singh et al. 2021). The code reproduces the line profiles assuming a molecular abundance relative to H_2, a source outer radius (r_{outer}, where the abundance drops by a factor of $1/e$), V_{LSR}, and the expansion velocity ($2V_{exp} = \Delta V_{1/2}$; see Table 2). A peak abundance is also modeled for the asymmetric flows. The level populations are calculated for ground and first vibrationally excited states. Data for energy levels were obtained from CDMS (Müller et al. 2005) and JPL (Pickett et al. 1998), while Einstein-A coefficients from Molecular Line Lists for Exoplanet and other Hot Atmospheres (EXOMOL; Tennyson & Yurchenko 2012) and CDMS, and collisional rates with H_2 from Ro-Vibrational Collisional Excitation Database and Utilities (BASECOL; Dubernet et al. 2010). A chi-squared test determined the best fits.

The radius of the star used for the analysis is $R_* = 2.4 \times 10^{14}$ cm (Monnier et al. 1997). The calculations are typically begun at $r_{inner} = 5 \times 10^{15}$ cm (~20 R_*), the approximate distance at which the envelope attains terminal velocity (Zubko et al. 2004). The abundance $f(r)$ is modeled by a Gaussian function, with the Gaussian parameters set by f_0 (maximum abundance), the e-folding radius r_{outer}, and for the nonspherical outflows, r_{peak}. Details about these expressions are fully described in Adande et al. (2013) and Singh et al. (2021). From the abundance function, spectra are generated. The fitting parameters are varied until the modeled spectra match the observed ones. The best fit is determined both qualitatively and with a chi-squared test. For the few narrow lines observed (NaCl, AlO), $r_{inner} \sim 10\ R_*$ was used instead. The dust infrared emission is modeled as a blackbody at $T_{dust} \sim 580$ K, assuming $T_* \sim 2500$ K (Zubko et al. 2004). Rotational levels in the ground and first vibrationally excited states are modeled by considering excitations due to collisions as well as infrared radiation from dust. A summary of model parameters is presented in Table 3.

Many of the observed line profiles appear to consist of a central, spherical component at the systemic velocity of the star, along with a narrow, blueshifted feature near $V_{LSR} = -21 \pm 3$ km s^{-1} and a broader, redshifted one near 15 ± 3 km s^{-1}. These latter two collimated outflows are randomly oriented, positioned ~34° and ~12°, respectively, from the line

Table 2
Molecules Identified in the Survey and Line Parameters[a]

Frequency (MHz)	Molecule	Transition	Component	Intensity (T_A^*(K))	$\Delta V_{1/2}$ (km s^{-1})[b]	V_{LSR} (km s^{-1})
214,689.4	SO_2	$J_{Ka,\ Kc} = 16_{3,13} \rightarrow 16_{2,14}$	Red	0.004 ± 0.001	15.3 ± 5.6	18.0 ± 5.6
			Spherical	0.009 ± 0.001	27.2 ± 5.6	-4.0 ± 2.8
			Blue	0.006 ± 0.001	12.5 ± 5.6	-22.5 ± 5.6
215,220.7	SO	$N_J = 5_5 \rightarrow 4_4$	Red	0.024 ± 0.001	16.2 ± 5.6	15.0 ± 5.6
			Spherical	0.024 ± 0.001	29.0 ± 5.6	-0.5 ± 5.6
			Blue	0.024 ± 0.001	10.0 ± 5.6	-16.5 ± 2.8
215,596.0	SiO, v = 1	$J = 5 \rightarrow 4$	Spherical	0.014 ± 0.001	39.0 ± 5.6	~ 7.0
215,839.9	^{34}SO	$N_J = 5_6 \rightarrow 4_5$	Red	~ 0.004	~ 15	~ 13.0
			Spherical	~ 0.005	~ 20	~ -0.5
			Blue	~ 0.003	~ 13	$\sim -12.$
216,531.4	$Na^{37}Cl$	$J = 17 \rightarrow 16$	Spherical	0.005 ± 0.001	13.8 ± 5.6	-1.5 ± 5.6
216,643.3	SO_2	$J_{Ka,Kc} = 22_{2,20} \rightarrow 22_{1,21}$	Combined	0.003 ± 0.001	~ 25	-3.5
216,710.4	H_2S	$J_{Ka,Kc} = 2_{2,0} \rightarrow 2_{1,1}$	Spherical	0.025 ± 0.001	22.4 ± 5.6	-1.0 ± 5.6
216,757.6	SiS, v = 1	$J = 12 \rightarrow 11$	Spherical	0.003 ± 0.001	20.1 ± 5.6	0.9 ± 5.6
217,105.0	SiO	$J = 5 \rightarrow 4$	Spherical	0.349 ± 0.001	35.2 ± 5.6	1.5 ± 5.6
$\sim$217, 520	U		Spherical	0.005 ± 0.002	~ 20	-1
217,817.7	SiS	$J = 12 \rightarrow 11$	Spherical	0.040 ± 0.001	37.3 ± 2.8	-1.0 ± 2.8
219,355.0	$^{34}SO_2$	$J_{Ka,Kc} = 11_{1,11} \rightarrow 10_{0,10}$	Combined	0.002 ± 0.001	51.9 ± 10.4	2.1 ± 5.6
219,949.4	SO	$N_J = 5_6 \rightarrow 4_5$	Red	0.049 ± 0.003	18.1 ± 2.8	19.5 ± 2.8
			Spherical	0.057 ± 0.003	28.5 ± 2.8	-2.0 ± 2.8
			Blue	0.057 ± 0.003	14.8 ± 2.8	-18 ± 2.8
220,398.7	^{13}CO	$J = 2 \rightarrow 1$	Combined	~ 0.08	~ 48	~ -1
221,260.2	NaCl	$J = 17 \rightarrow 16$	Spherical	0.010 ± 0.002	15.9 ± 2.7	0.5 ± 2.7
221,965.2	SO_2	$J_{Ka,Kc} = 11_{1,11} \rightarrow 10_{0,10}$	Red	0.020 ± 0.002	12.2 ± 2.7	16.5 ± 2.7
			Spherical	0.019 ± 0.002	25.8 ± 2.7	-1.5 ± 2.7
			Blue	0.037 ± 0.002	9.2 ± 2.7	-20.8 ± 2.7
225,153.7	SO_2	$J_{Ka,Kc} = 13_{2,12} \rightarrow 13_{1,13}$	Red	0.011 ± 0.002	17.8 ± 2.7	17.0 ± 2.7
			Spherical	0.010 ± 0.002	30.1 ± 2.7	-4.0 ± 2.7
			Blue	0.014 ± 0.002	10.3 ± 2.7	-22.0 ± 2.7
			Red	0.006 ± 0.001	13.0 ± 5.6	18.0 ± 5.6
226,300.0	SO_2	$J_{Ka,Kc} = 14_{3,13} \rightarrow 14_{2,13}$	Spherical	0.006 ± 0.001	29.5 ± 5.6	-1.0 ± 2.8
			Blue	0.006 ± 0.001	9.0 ± 5.6	-19.0 ± 5.6
226,658.9[d]	CN	$N, J = 2, 3/2 \rightarrow 1, 1/2$	Spherical	~ 0.004	~ 50	~ 0
226,876.5[d]	CN	$N, J = 2, 3/2 \rightarrow 1, 1/2$	Spherical	0.007 ± 0.002	36.8 ± 5.2	~ 1.5
227,589.9	^{30}SiS	$J = 13 \rightarrow 12$	Spherical	0.002 ± 0.001	52.9 ± 10.4	-1.0 ± 5.6
229,246.0	$Na^{37}Cl$	$J = 18 \rightarrow 17$	Spherical	0.006 ± 0.001	14.0 ± 2.6	-1.5 ± 2.6
229,500.8	$Si^{34}S$	$J = 13 \rightarrow 12$	Spherical	0.002 ± 0.001	25.2 ± 5.2	-1.3 ± 5.2
230,538.0	CO	$J = 2 \rightarrow 1$[e]	Red	~ 0.75	~ 13	~ 20
			Spherical	~ 0.80	~ 32	~ 1.5
			Blue	~ 0.55	~ 9	~ -19
231,626.7	^{29}SiS	$J = 13 \rightarrow 12$	Spherical	0.004 ± 0.002	23.4 ± 7.8	-1.0 ± 5.6
234,251.8	NaCl	$J = 18 \rightarrow 17$	Spherical	0.018 ± 0.001	14.7 ± 2.6	0.5 ± 2.6
234,935.7	PN	$J = 5 \rightarrow 4$	Spherical	~ 0.005	~ 9.1	~ -1.0
235,151.7	SO_2	$J_{Ka,Kc} = 4_{2,2} \rightarrow 3_{1,3}$	Red	0.015 ± 0.002	13.8 ± 2.6	15.0 ± 2.8
			Spherical	0.010 ± 0.002	28.6 ± 2.6	-1.0 ± 2.8
			Blue	0.017 ± 0.002	11.8 ± 2.8	-21 ± 2.8
235,380.0	U	...	Spherical	~ 0.08	~ 48	~ -1
235,961.4	SiS	$J = 13 \rightarrow 12$	Spherical	0.041 ± 0.002	35.9 ± 2.5	0.1 ± 2.5
236,216.7	SO_2	$J_{Ka,Kc} = 11_{1,11} \rightarrow 10_{0,10}$	Red	0.009 ± 0.002	9.8 ± 5.0	14.0 ± 5.0
			Spherical	0.010 ± 0.002	20.8 ± 2.7	-3.0 ± 2.7
			Blue	0.010 ± 0.002	9.5 ± 2.7	-21.5 ± 2.7
237,068.8	SO_2	$J_{Ka,Kc} = 12_{3,9} \rightarrow 12_{2,10}$	Red	0.009 ± 0.002	17.3 ± 5.0	15.0 ± 5.0
			Spherical	0.01 ± 0.002	30.3 ± 5.0	-2.0 ± 2.7
			Blue	0.008 ± 0.002	9.0 ± 5.0	-20.5 ± 5.0
239,953.6[d]	PO	$J = 11/2 \rightarrow 9/2$, e; $\Omega = 1/2$	Spherical	~ 0.004	~ 12	~ -1.5
240,146.8[d]	PO	$J = 11/2 \rightarrow 9/2$, f; $\Omega = 1/2$	Spherical	~ 0.002	~ 50	~ -1.5
240,942.8	SO_2	$J_{Ka,Kc} = 18_{1,17} \rightarrow 18_{0,18}$	Combined	~ 0.007	~ 37.6	~ -1.5
241,615.8	SO_2	$J_{Ka,Kc} = 5_{2,4} \rightarrow 4_{1,3}$	Red	0.015 ± 0.001	13.5 ± 2.5	13.5 ± 2.5
			Spherical	0.014 ± 0.001	28.3 ± 2.5	-1.5 ± 2.5
			Blue	0.024 ± 0.001	10.5 ± 2.5	-20.8 ± 2.5
241,956.8	$Na^{37}Cl$	$J = 19 \rightarrow 18$	Spherical	0.006 ± 0.001	15.4 ± 2.5	-2.8 ± 2.5
242,095.0	$Si^{18}O$	$J = 6 \rightarrow 5$	Spherical	0.004 ± 0.001	33.2 ± 5.0	-0.3 ± 5.0
243,087.6	SO_2	$J_{Ka,Kc} = 5_{4,2} \rightarrow 6_{3,3}$	Combined	~ 0.003	~ 27.5	~ -2
244,254.2	SO_2	$J_{Ka,Kc} = 14_{0,14} \rightarrow 13_{1,13}$	Red	0.015 ± 0.001	15.2 ± 2.5	14.0 ± 2.5

Table 2
(Continued)

Frequency (MHz)	Molecule	Transition	Component	Intensity (T_A^*(K))	$\Delta V_{1/2}$ (km s^{-1})[b]	V_{LSR} (km s^{-1})
			Spherical	0.015 ± 0.001	26.0 ± 2.5	−2.5 ± 2.5
			Blue	0.027 ± 0.001	9.1 ± 4.8	−22.0 ± 2.5
244,935.6	CS	$J = 5 \rightarrow 4$	Red	0.013 ± 0.002	14.5 ± 2.5	11.5 ± 2.5
			Spherical	0.013 ± 0.002	27.5 ± 2.5	0.0 ± 2.5
			Blue	0.009 ± 0.002	10.0 ± 2.5	−23 ± 2.5
245,088.4	^{30}SiS	$J = 14 \rightarrow 13$	Spherical	0.003 ± 0.002	24.9 ± 5.0	−3.0 ± 5.0
245,401.1	NaCl, v = 1	$J = 19 \rightarrow 18$	Spherical	0.005 ± 0.002	7.2 ± 2.5	−1.5 ± 2.5
245,563.4	SO_2	$J_{Ka,Kc} = 10_{3,7} \rightarrow 10_{2,8}$	Red	0.010 ± 0.002	∼14	∼13.5
			Spherical	0.018 ± 0.002	∼25	∼−2.0
			Blue	0.018 ± 0.002	∼10	∼−21.5
247,239.6	NaCl	$J = 19 \rightarrow 18$	Spherical	0.012 ± 0.002	12.3 ± 2.5	−0.5 ± 2.5
248,057.4	SO_2	$J_{Ka,Kc} = 15_{2,14} \rightarrow 15_{1,15}$	Red	0.007 ± 0.002	17.5 ± 4.8	16.0 ± 4.8
			Spherical	0.009 ± 0.002	30.5 ± 4.8	1.0 ± 4.8
			Blue	0.015 ± 0.002	8.5 ± 2.5	−22.0 ± 2.5
249,435.4	^{29}SiS	$J = 14 \rightarrow 13$	Spherical	0.004 ± 0.002	24.3 ± 4.8	0.5 ± 5.0
251,205.1[c]	SO_2	$J_{Ka,Kc} = 13_{1,13} \rightarrow 12_{0,12}$ $J_{Ka,Kc} = 8_{3,5} \rightarrow 8_{2,6}$	Combined	∼0.044	∼44	∼−2.3
251,825.8	SO	$N_J = 6_5 \rightarrow 5_4$	Red	0.028 ± 0.002	12.9 ± 4.8	15.0 ± 4.8
			Spherical	0.033 ± 0.002	26.0 ± 4.8	−3.1 ± 4.8
			Blue	0.032 ± 0.002	9.1 ± 4.8	−18.9 ± 4.8
253,571.0[d]	NS	$J = 11/2 \rightarrow 9/2$ c	Spherical	0.003 ± 0.001	33.0 ± 5.6	∼−1.0
253,739.8	$SO^{18}O$	$J_{Ka,Kc} = 14_{3,12} \rightarrow 13_{3,11}$	Spherical	∼0.003	∼25	∼−1.5
253,969.8[d]	NS	$J = 11/2 \rightarrow 9/2$ d	Spherical	0.004 ± 0.001	40.0 ± 5.6	∼−1.0
254,103.2	SiS	$J = 14 \rightarrow 13$	Spherical	0.048 ± 0.001	36.5 ± 2.4	−1.6 ± 2.4
254,216.7	^{30}SiO	$J = 6 \rightarrow 5$	Spherical	0.049 ± 0.001	37.2 ± 2.4	0.0 ± 2.4
254,281.9	SO_2	$J_{Ka,Kc} = 6_{3,3} \rightarrow 6_{2,4}$	Red	0.010 ± 0.001	∼13	∼18
			Spherical	0.010 ± 0.001	∼26	∼−1
			Blue	0.014±0.001	∼~8	∼−19
254,663.2	$Na^{37}Cl$	$J = 20 \rightarrow 19$	Spherical	0.008 ± 0.002	14.2 ± 2.4	2.8 ± 2.4
255,553.3	SO_2	$J_{Ka,Kc} = 4_{3,1} \rightarrow 4_{2,2}$	Red	0.006 ± 0.002	14.8 ± 4.6	16.5 ± 4.6
			Spherical	0.009 ± 0.002	16.2 ± 4.6	−1.5 ± 2.4
			Blue	0.020 ± 0.002	10.0 ± 4.6	−21.0 ± 4.6
255,958.0	SO_2	$J_{Ka,Kc} = 3_{3,1} \rightarrow 3_{2,2}$	Red	0.007 ± 0.002	16.2 ± 4.6	12.0 ± 4.6
			Spherical	0.01 ± 0.002	18.8 ± 4.6	−1.5 ± 2.4
			Blue	0.012 ± 0.002	12.0 ± 4.6	−20.0 ± 4.6
256,246.9	SO_2	$J_{Ka,Kc} = 5_{3,3} \rightarrow 5_{2,4}$	Red	0.005 ± 0.002	13.4 ± 4.6	14.0 ± 4.6
			Spherical	0.009 ± 0.002	13.6 ± 4.6	−2.0 ± 4.6
			Blue	0.020 ± 0.002	23.5 ± 4.6	−20.0 ± 4.6
256,877.5[c]	^{34}SO	$N_J = 7_6 \rightarrow 6_5$	Combined	∼0.007	∼35	∼−1
256,898.4[c]	SiO v = 2	$J = 6 \rightarrow 5$	Spherical	∼0.022	∼13	∼−2
257,100.0	SO_2	$J_{Ka,Kc} = 7_{3,5} \rightarrow 7_{2,6}$	Red	0.014 ± 0.002	14.9 ± 4.6	17.0 ± 4.6
			Spherical	0.013 ± 0.002	27.5 ± 4.6	−2 ± 4.6
			Blue	0.023 ± 0.002	9.3 ± 4.6	−19.5 ± 4.6
257,255.2	^{29}SiO	$J = 6 \rightarrow 5$	Spherical	0.080 ± 0.002	36.4 ± 2.3	0.4 ± 2.3
258,255.8	SO	$N_J = 6_6 \rightarrow 5_5$	Red	0.035 ± 0.003	13.3 ± 4.6	16.7 ± 4.6
			Spherical	0.038 ± 0.003	23.5 ± 4.6	−1.0 ± 4.6
			Blue	0.040 ± 0.003	8.5 ± 4.8	−19.0 ± 4.8
258,707.4	SiO v = 1	$J = 6 \rightarrow 5$	Spherical	0.028 ± 0.002	22.7 ± 4.6	−0.5 ± 4.6
258942.2	SO_2	$J_{Ka,Kc} = 9_{3,\ 7} \rightarrow 9_{2,\ 8}$	Red	0.014 ± 0.002	13.8 ± 4.6	12.0 ± 4.6
			Spherical	0.013 ± 0.002	25.4 ± 4.6	−0.5 ± 4.6
			Blue	0.023 ± 0.002	10.3 ± 4.6	−19.5 ± 4.6
259011.8	$H^{13}CN$	$J = 3 \rightarrow 2$	Spherical	0.029 ± 0.002	46.8 ± 4.6	−1.0 ± 4.6
260223.1	NaCl	$J = 20 \rightarrow 19$	Spherical	0.018 ± 0.002	14.1 ± 2.3	−2.5 ± 4.6
260518.0	SiO	$J = 6 \rightarrow 5$	Spherical	0.451 ± 0.002	33.6 ± 2.3	1.1 ± 2.3
261843.7	SO	$N_J = 6_7 \rightarrow 5_6$	Red	0.078 ± 0.003	14.0 ± 4.6	15.0 ± 4.6
			Spherical	0.082 ± 0.003	25.5 ± 4.6	−1.5 ± 4.6
			Blue	0.065 ± 0.003	11.0 ± 4.8	−19.0 ± 4.8
262256.9	SO_2	$J_{Ka,Kc} = 11_{3,\ 9} \rightarrow 11_{2,\ 10}$	Red	0.011 ± 0.002	16.0 ± 4.6	14.0 ± 4.6
			Spherical	0.013 ± 0.002	24.5 ± 4.6	0.0 ± 4.6
			Blue	0.023 ± 0.002	10.5 ± 4.6	−22.0 ± 4.6
262,585.0	^{30}SiS	$J = 15 \rightarrow 14$	Spherical	0.004 ± 0.001	25.8 ± 4.6	−1.0 ± 4.6
264,789.7	$Si^{34}S$	$J = 15 \rightarrow 14$	Spherical	0.004 ± 0.001	30.9 ± 4.6	−1.0 ± 4.6
265,886.4	HCN	$J = 3 \rightarrow 2$	Spherical	0.240 ± 0.002	39.1 ± 4.6	−1.0 ± 4.6
267200.2	HCN, $v_2 = 1$	$J = 3 \rightarrow 2$	Spherical	0.005 ± 0.002	14.9 ± 4.6	−1.0 ± 4.6

Table 2
(Continued)

Frequency (MHz)	Molecule	Transition	Component	Intensity (T_A^*(K))	$\Delta V_{1/2}$ (km s^{-1})[b]	V_{LSR} (km s^{-1})
267,242.2	^{29}SiS	$J = 15 \rightarrow 14$	Spherical	~ 0.005	~ 20	~ 0.1
267,365.8	Na^{37}Cl	$J = 21 \rightarrow 20$	Spherical	0.007 ± 0.002	6.1 ± 2.3	-3.5 ± 2.3
267,537.5	SO_2	$J_{Ka,Kc} = 13_{3,11} \rightarrow 13_{2,12}$	Red	0.006 ± 0.001	13.8 ± 2.3	16.0 ± 2.3
			Spherical	0.011 ± 0.001	27.2 ± 2.3	-1.5 ± 2.3
			Blue	0.015 ± 0.001	10.2 ± 2.3	-20.5 ± 2.3
267,557.6	HCO^+	$J = 3 \rightarrow 2$	Blue	~ 0.002	⋯	⋯
			Red	~ 0.003	⋯	⋯
267,716.9	U	⋯	Spherical	0.004 ± 0.001	~30	-1
267,937.0[c]	AlO	$N = 7 \rightarrow 6$	Spherical	~ 0.002	~ 10	~ -1
268,149.2	H_2O $v_2 = 2$	$J_{Ka,Kc} = 6_{5,2} \rightarrow 7_{4,3}$	Combined	~ 0.002	~ 34	~ -1
268,180.0	U	⋯	Spherical	~ 0.002	~ 20	-1
270,918.0	SiS $v = 1$	$J = 15 \rightarrow 14$	Spherical	0.058 ± 0.002	16.0 ± 2.2	-1.0 ± 2.3
271,529.0	SO_2	$J_{Ka,Kc} = 7_{2,6} \rightarrow 6_{1,5}$	Red	0.013 ± 0.003	13.1 ± 2.2	17.0 ± 2.2
			Spherical	0.015 ± 0.002	22.5 ± 2.2	-0.5 ± 2.2
			Blue	0.018 ± 0.002	9.4 ± 2.2	-21.5 ± 2.2
271,981.1	HNC	$J = 3 \rightarrow 2$	Spherical	0.007 ± 0.001	45.0 ± 8.8	1.9 ± 8.8
272,243.1	SiS	$J = 15 \rightarrow 14$	Spherical	0.048 ± 0.003	34.8 ± 2.2	-0.9 ± 2.2
273,202.0	NaCl	$J = 21 \rightarrow 20$	Spherical	0.014 ± 0.002	14.1 ± 2.2	-1.6 ± 2.2
275,240.2	SO_2	$J_{Ka,Kc} = 15_{3,13} \rightarrow 15_{2,14}$	Combined	~ 0.010	~ 37	~ -2.7
280,063.7	Na^{37}Cl	$J = 22 \rightarrow 21$	Spherical	0.009 ± 0.002	12.8 ± 4.3	-3.0 ± 4.3
280,079.7	^{30}SiS	$J = 16 \rightarrow 15$	Spherical	0.005 ± 0.002	31.3 ± 4.3	-0.3 ± 4.3
281,762.6	SO_2	$J_{Ka,Kc} = 15_{1,15} \rightarrow 14_{0,14}$	Red	0.021 ± 0.001	12.7 ± 4.2	13.5 ± 4.2
			Spherical	0.025 ± 0.001	21.5 ± 4.2	-2.0 ± 4.2
			Blue	0.039 ± 0.001	10.0 ± 4.2	-22.0 ± 4.2
281,914.2	PN	$J = 6 \rightarrow 5$	Spherical	0.005 ± 0.002	~ 48	~ -2.0
282,036.6	SO_2	$J_{Ka,Kc} = 20_{1,19} \rightarrow 20_{0,20}$	Red	0.015 ± 0.002	15.1 ± 4.2	15.5 ± 4.2
			Spherical	0.015 ± 0.002	27.5 ± 4.2	-3.0 ± 4.2
			Blue	0.024 ± 0.002	13.4 ± 4.2	-22.5 ± 4.2
282,431.2[c]	Si^{34}S	$J = 16 \rightarrow 15$	Spherical	0.010 ± 0.002	37.1 ± 2.1	-1.0 ± 4.2
282,434.7[c]	Si^{18}O	$J = 7 \rightarrow 6$				
283,183.6	$^{34}SO_2$	$J_{Ka,Kc} = 16_{0,16} \rightarrow 15_{1,15}$	Spherical	~ 0.004	~ 40	~ -1
283,464.8	SO_2	$J_{Ka,Kc} = 16_{0,14} \rightarrow 15_{1,15}$	Red	0.018 ± 0.002	14.5 ± 4.2	15.0 ± 4.2
			Spherical	0.021 ± 0.002	29.1 ± 4.2	-2.0 ± 4.2
			Blue	0.045 ± 0.002	9.1 ± 4.2	-21.5 ± 4.2
283,590.0[d]	PO	$J = 13/2 \rightarrow 11/2$, e; $\Omega = 1/2$	Spherical	0.006 ± 0.003	14.7 ± 4.2	0.6 ± 4.2
283,781.5[d]	PO	$J = 13/2 \rightarrow 11/2$, f; $\Omega = 1/2$	Spherical	0.004 ± 0.003	22.4 ± 6.3	0.3 ± 6.3
284,047.6	NaCl $v = 1$	$J = 22 \rightarrow 21$	Spherical	0.007 ± 0.003	7.5 ± 2.1	1.0 ± 2.1
285,047.0	^{29}SiS	$J = 16 \rightarrow 15$	Spherical	0.006 ± 0.002	43.7 ± 6.3	0.3 ± 6.3

Notes.
[a] Uncertainty range is $\pm 1.5\sigma$, measured from 2 MHz resolution data; frequencies given are measured.
[b] FWHM.
[c] Blended lines.
[d] Blend of hyperfine components; average frequency given.
[e] Galactic contamination removed.

Table 3
Modeling Parameters for NML Cyg

Distance (kpc)	$\dot{M}$ ($M_\odot$ yr^{-1})	R_*(cm)	V_{LSR} (km s^{-1})	T_{dust} (K)	T_{gas}	γ
1.6	10^{-4}	2.4×10^{14}	-1	580	$270\left(\frac{10^{16}}{r}\right)^{\gamma}$	0.5

of sight; they likely trace sporadic mass-loss events in NML Cyg (Singh et al. 2021). As a consequence, many of the molecular lines observed were fit with this three-component model. These components are indicated in the table as "Spherical," "Red," and "Blue." Line profiles where there was little evidence for multiple components were simply fit with the spherical model; those features where three components were likely present but were difficult to accurately analyze, were labeled "Combined." For other spectra, where the signal-to-noise was insufficient for the modeling, or there were blended features, only estimates of the line parameters are given.

Figure 3 displays example fits to the line profiles, using ESCAPADE. Additional examples can be found in

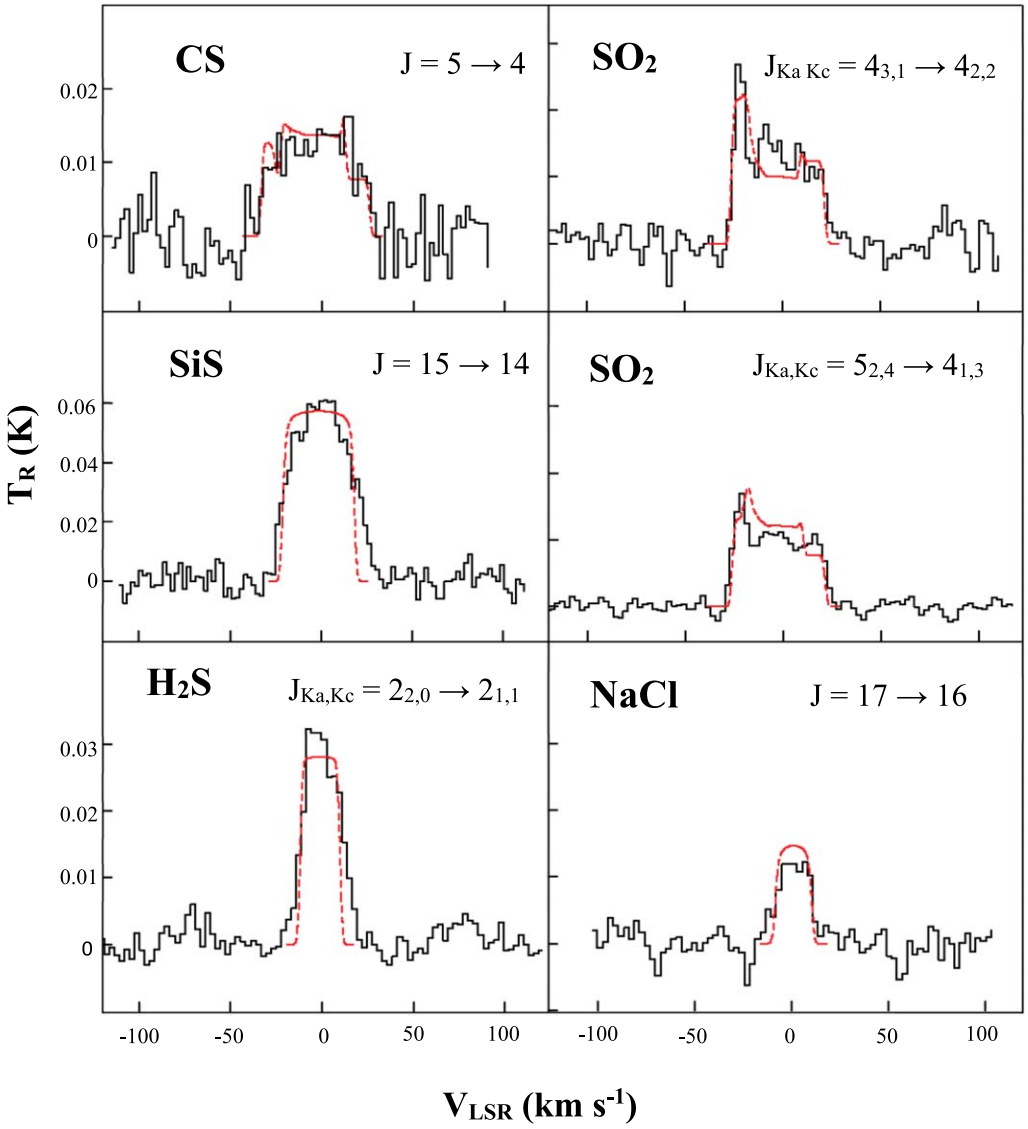

Figure 3. Spectra of CS ($J = 5 \rightarrow 4$), SiS ($J = 15 \rightarrow 14$), H_2S ($J_{Ka,Kc} = 2_{2,0} \rightarrow 2_{1,1}$), SO_2 ($J_{Ka,Kc} = 4_{3,1} \rightarrow 4_{2,2}$), SO_2 ($J_{Ka,Kc} = 5_{2,4} \rightarrow 4_{1,3}$), and NaCl ($J = 17 \rightarrow 16$), observed in the survey of NML Cyg (in black), overlayed with the model profile from the ESCAPADE analysis (in dashed red or gray scale). Temperature scale in T_R (K). CS and SO_2 was modeled with three velocity components (spherical outflow, redshifted wind, and blueshifted flow; see text), while NaCl, SiS, and H_2S were fit with only a single, spherical component. The line profile of NaCl is narrower than the other molecules. Spectral resolution in 2 MHz.

Singh et al. (2021). In this figure, observed spectra of CS ($J = 5 \rightarrow 4$), SiS ($J = 15 \rightarrow 14$), H_2S ($J_{Ka,Kc} = 2_{2,0} \rightarrow 2_{1,1}$), SO_2 ($J_{Ka,Kc} = 4_{3,1} \rightarrow 4_{2,2}$ and $5_{2,4} \rightarrow 4_{1,3}$), and NaCl ($J = 17 \rightarrow 16$), are shown, overlayed with the modeled profile (in red or gray scale). Here, CS and SO_2 were modeled with the aforementioned three velocity components (red, blue, and spherical), as suggested by their broad line profiles. The other three species, NaCl, SiS, and H_2S, were fit with only the spherical flow. Although SiS lines sometimes appeared somewhat asymmetric, it was difficult to discern individual velocity components. The lines of NaCl, on the other hand, clearly consisted of a single, narrow component. The observation of multiple transitions of NaCl and SiS helped to constrain the model parameters of the spherical flow. As the figure shows, the observed profiles are well produced by the modeling. The lines of NaCl helped to constrain the systemic velocity of the source, which, within the uncertainties, is $V_{LSR} = -1$ km s^{-1}. This velocity was found for almost all observed lines. SiS and H_2S lines gave a good estimate of line width for molecules traversing the spherical flow. The analysis of most molecules consistently produced a terminal expansion velocity of $V_{exp} \approx 16 \pm 3$ km s^{-1}, in good agreement with current literature (Richards et al. 1996; Danchi et al. 2001; Zubko et al. 2004).

From the ESCAPADE modeling, the approximate radial extent of the individual molecular distributions is determined. Figure 4 presents these radial distributions for the molecules detected in this survey for the spherical outflow. Figure 5 shows the radial distribution in blue and red outflows. For these components, only SO, SO_2, CS, CO, and HCO^+ were modeled because distinct velocity components were visible in their spectra, and the data for most lines of these molecules had reasonable signal-to-noise ratios.

4. Discussion

4.1. Overall Chemistry in NML Cygni

Of the 104 emission features observed in the 1 mm spectrum of NML Cyg, 32 of them arise from SO_2 and its isotopologues.

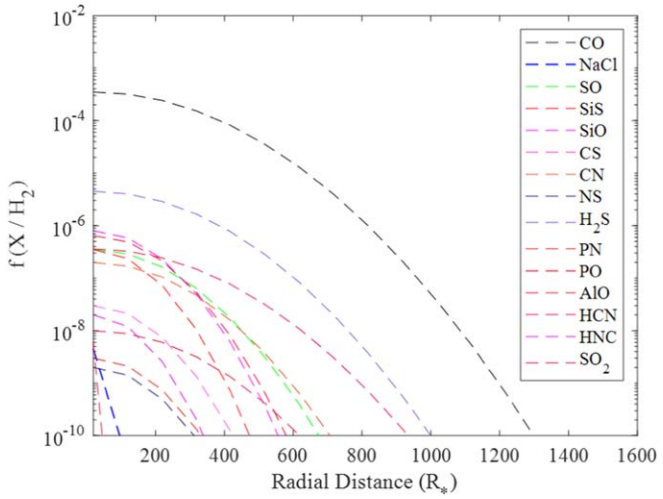

Figure 4. Radial abundance plots for the molecules in the spherical outflow of the envelope of NML Cyg, derived from the modeling. The abundances were extrapolated from their maximum values at $r_{\rm inner}$ to $f \sim 10^{-10}$, assuming a Gaussian centered at $r_{\rm inner}$ ($\sim$20 R_*; see text). As the figure shows, CO, HCN, and H_2S are the most extended molecules in the envelope.

The next most prominent species is silicon monosulfide, SiS, which accounts for 17 lines, including those arising from the v = 1 vibrational state, and isotopologues (^{29}SiS, ^{30}SiS, and Si^{34}S). These two molecules account for nearly half of the total emission features observed. A similar situation has been found in the 1 mm spectrum of VY CMa (Tenenbaum et al. 2010a, 2010b). Also analogous to VY CMa, only diatomics and triatomics were observed in the 1 mm band, although the four-atom molecule NH_3 has been identified on both envelopes (e.g., Teyssier et al. 2012). Overall, eight molecules contain oxygen, six contain sulfur, six contain carbon, five contain nitrogen, two contain phosphorous, two contain silicon, one contains aluminum, and one contains sodium and chlorine.

The spherical outflow contains the most molecules and therefore best represents the overall chemistry of NML Cyg. From the ESCAPADE modeling, CO was found to have the highest abundance, relative to H_2, in the survey, with $f \sim 3.5 \times 10^{-4}$. The carbon is apparently contained primarily in CO, with the remaining sequestered with sulfur and nitrogen. CN and HCN also contain significant amounts of carbon, with $f \sim 2.0 \times 10^{-7}$ and 3.6×10^{-7}, respectively. The abundances of the C-bearing species CS ($f \sim 3.0 \times 10^{-8}$) and HNC ($f \sim 2.0 \times 10^{-8}$) are about 1 order of magnitude lower. Nitrogen in NML Cyg exists primarily as HCN, HNC, CN, and NS. The [HCN]/[HNC] ratio is >18. HCN is optically thick ($\tau \sim 1$) in NML Cyg—similar to another O-rich star IK Tauri (Velilla Prieto et al. 2017). Therefore, this value is an upper limit, but still appears to be significantly less than what is found in C-rich envelopes ([HCN]/[HNC] $\sim$ 40–300; Woods et al. 2003). It is also noteworthy that a major transition of NO exists in the 1 mm band, but is not observed, while lines of NS have been detected. The silicon-containing molecules SiO and SiS are also prevalent, with $f \sim 8 \times 10^{-7}$ and 4.5×10^{-7}. Sulfur is principally contained in oxides ($f(SO) \sim 3.5 \times 10^{-7}$; $f(SO_2) \sim 6.5 \times 10^{-7}$) and hydrides ($f(H_2S) \sim 4.5 \times 10^{-6}$). The most prominent carrier of this element in NML Cyg is H_2S. NS is a minor sulfur-bearing constituent with $f \sim 2 \times 10^{-9}$. Phosphorus is well represented by PO, which has the highest abundance of the more refractory species ($f \sim 10^{-8}$), and also by PN ($f \sim 3.0 \times 10^{-9}$). The metal-bearing molecules AlO and NaCl have abundances of 6×10^{-9} and 4.5×10^{-9} (also see Table 4).

Given the derived abundances, carbon appears to be contained primarily in CO, within our uncertainties. Note that the solar abundance of carbon is 2.7×10^{-4} (Asplund et al. 2009). CO is also a major oxygen carrier, given the solar abundance of O of 4.8×10^{-4} (Asplund et al. 2009). The remainder of the oxygen may be in the form of H_2O, for which we have little information from our survey.

The chemistry of NML Cyg resembles that of other hypergiant stars, VY CMa and IRC+10420, although the latter source has some noticeable differences from the other two envelopes (Quintana-Lacaci et al. 2016a; Ziurys et al. 2007, 2009). As shown in Table 4, carbon is contained in the same six molecules in all three sources (CO, CS, CN, HCN HCO^+, and HNC), except that CH_3OH is also apparently present in IRC+10420. CO is about a factor of 10 less prevalent in VY CMa as opposed to the other two sources, based on the spherical wind, while HCN and CS are within a factor of 3 for all envelopes. The three envelopes contain similar abundances for SO, SO_2, and CS, within factors of 2–3: see Table 4. SO_2 and SO have $f \sim 3$–6×10^{-7} and $f \sim 0.3$–1×10^{-6}, respectively, in all three objects. The abundance of CS is somewhat lower relative to the other S-bearing molecules in the three hypergiants, with $f \sim 0.3$–2×10^{-7}, as might be expected in O-rich gas. H_2S is present in NML Cyg and VY CMa, but not IRC+10420. Among the refectory molecules, NaCl and AlO were detected in NML Cyg and VY CMa, where the abundances are comparable, but not in IRC+120420. PN was seen in all three sources; abundances fall in the range 0.4–4 $\times 10^{-8}$. Note that the abundances for IRC+10420 were derived using rotational diagrams, not a radiative transfer code (Quintana-Lacaci et al. 2016a). Qualitative comparisons are therefore only appropriate.

The comparison with O-rich AGB stars is more complicated, because many more such objects have been studied. Abundances therefore have a larger spread of values, as shown in Table 4. Again, we note that the abundances for IK Tau from Velilla Prieto et al. (2017) were derived using rotational diagrams, not a radiative transfer code, making direct comparisons only qualitative. As shown in Table 4, the supergiant abundances fall in the ranges found for the AGB stars. For some AGB envelopes, however, abundances for HCN, H_2S, SO, SO_2, and even NaCl are higher than those found for supergiants. Phosphorous, represented by PN and PO, is common in O-rich envelopes, both in AGB stars and hypergiants, although there are some variations (Ziurys et al. 2018). For example, PO has not been found in IRC+10420.

Based on NML Cyg and VY CMa, sulfur also apparently plays a critical role in tracing the outflow structures in hypergiant envelopes. After CO, only SO, SO_2, and CS clearly trace all outflow components. It is likely that other molecules do as well, but their overall abundances are much lower.

4.2. Radial Distribution of the Molecules

A detailed picture of the chemistry is perhaps elucidated by the radial distribution plots found in Figures 4 and 5. For all three winds, the abundance distribution is modeled as a Gaussian, except the spherical wind has the maximum at $r_{\rm inner}$, and the directed outflows at $r_{\rm peak}$ (see Singh et al. 2021; Adande et al. (2013). The Gaussian model allows the abundance to be calculated at any radius from the star; the

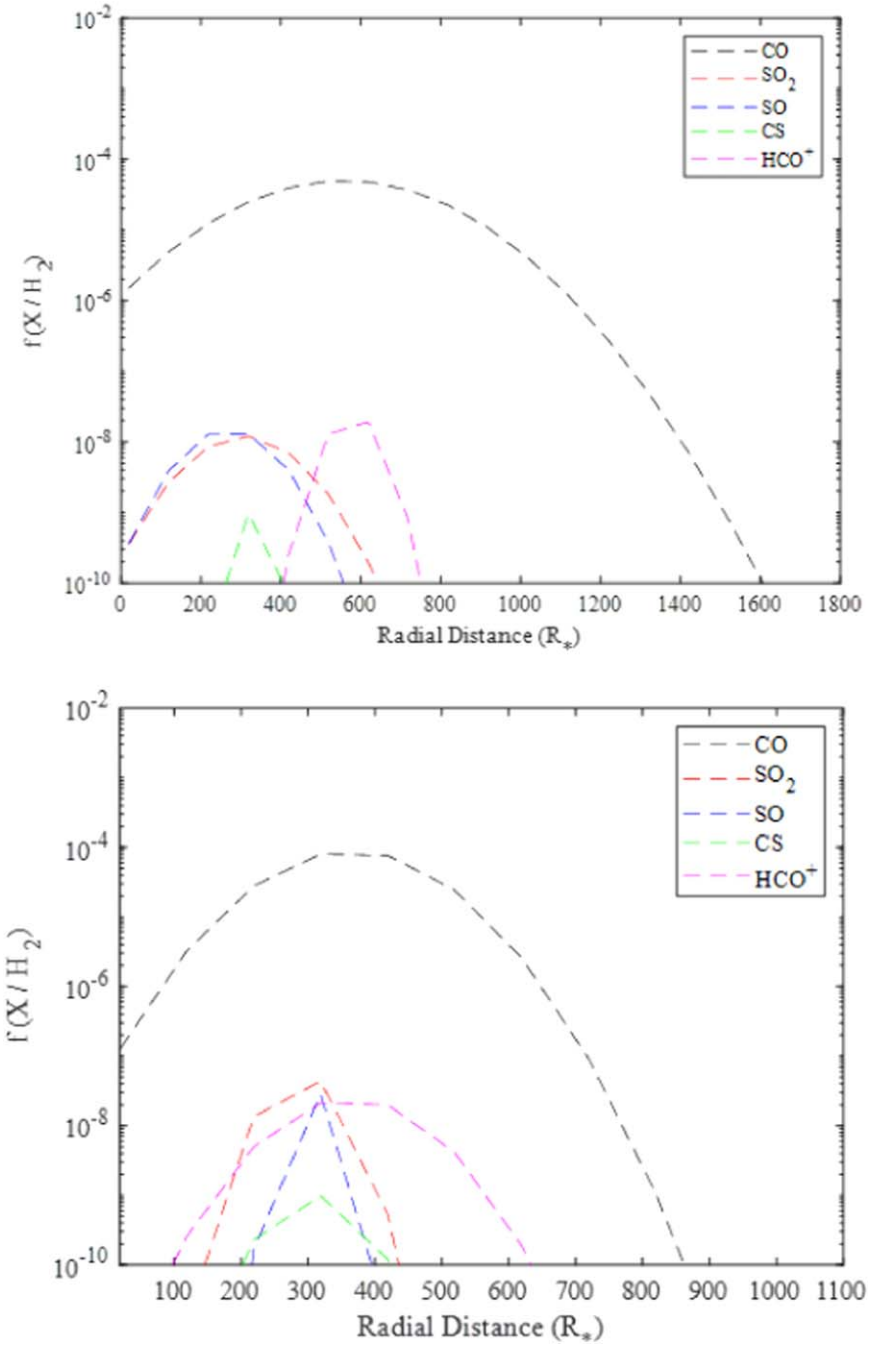

Figure 5. Radial abundance plots for the molecules in the blueshifted wind (upper) and redshifted flow (lower) for the envelope of NML Cyg, derived from the modeling. The abundances were extrapolated from their maximum values to $f \sim 10^{-10}$, assuming a distribution Gaussian centered at the peak (see text). As is evident in the figure, CO has the largest extent in these directed outflows, and is followed by HCO^+. The three sulfur-bearing species CS, SO, and SO_2 lie closer to the star and appear to have correlated abundances.

figures display the abundance distribution to $f \sim 10^{-10}$. For the spherical wind (see Figure 4), CO has the furthest extent, reaching an e-folding radius of $\sim 330\, R_*$ (Singh et al. 2021), which extrapolates to $\sim$1200 R_*. This result is perhaps expected, given the low dipole moment of this molecule and the possible self-shielding effect of CO that prevents its photodissociation (Saberi et al. 2019). HCN and H_2S are also extended, with $r_{\rm outer} \sim 320$ and 300 R_*, reaching a distance of $\sim$1000 R_*. In contrast, NaCl and AlO have radii of $r_{\rm outer} < 50\, R_*$, with abundances that drop quickly with increasing radius. This result is consistent with their lower expansion velocities (see Table 2), which indicate that these molecules condense out in the dust formation zone (e.g., Tenenbaum et al. 2010a, 2010b). The radial distributions of the other molecules lie in between these two extremes, with distributions characterized by $r_{\rm outer} \sim 140$–$280\, R_*$, and extending out to $\sim$300–700 R_* with decreased abundance.

For the collimated outflows, both red- and blueshifted winds show similar characteristics; however, the red outflow extends further from the star by about $\sim$500 R_*. CO is clearly the molecule with the largest source sizes, with $r_{\rm peak} \sim 560$ and 365 R_* and $r_{\rm outer} \sim 860$ and 650 R_*, for the red and blueshifted

Table 4
Representative Abundances in O-rich Circumstellar Envelopes[a]

Molecule	NML Cyg	Hypergiants[b]	O-rich AGB Stars[c]
CO	$\sim 3.5 \times 10^{-4}$	$0.4–5.3 \times 10^{-4}$	$1–5 \times 10^{-4}$
HCN	$\sim 3.6 \times 10^{-7}$	$\sim 10^{-6}$	$0.9–9 \times 10^{-6}$
H_2S	4.5×10^{-6}	4×10^{-7}	$0.04–2.5 \times 10^{-5}$
SO	3.5×10^{-7}	$0.3–1 \times 10^{-6}$	10^{-6}
SO_2	6.5×10^{-7}	3×10^{-7}	10^{-6}
CS	3.0×10^{-8}	$1–2 \times 10^{-7}$	$0.07–8 \times 10^{-7}$
NaCl	4.5×10^{-9}	5×10^{-9}	$0.05–3.1 \times 10^{-7}$
PN	3.9×10^{-9}	$0.7–4 \times 10^{-8}$	$1–2 \times 10^{-8}$
AlO	$\sim 6 \times 10^{-9}$	10^{-8}	5×10^{-9}

Notes.
[a] Relative to H_2.
[b] Quintana-Lacaci et al. (2016a; rotational diagram analysis only); Ziurys et al. (2007, 2009).
[c] Danilovich et al. (2017); Danilovich et al. (2019, 2020); Velilla Prieto et al. (2017; rotational diagram analysis only); Ziurys et al. (2009); Milam et al. (2007); De Beck et al. (2017); Kaminski et al. (2016).

Table 5
Isotope Ratios in NML Cyg

Isotopes	NML Cyg[a]	Solar[b]
$^{28}Si/^{29}Si$	33 ± 10	20
$^{28}Si/^{30}Si$	33 ± 10	29
$^{29}Si/^{30}Si$	1.2 ± 1.0	1.5
$^{32}S/^{34}S$	50 ± 25	25
$^{12}C/^{13}C$	33 ± 15	89
$^{16}O/^{18}O$	>250	500
$^{35}Cl/^{37}Cl$	3.9 ± 0.3	3.13

Notes.
[a] Sulfur and silicon derived from SiS, carbon from HCN, oxygen from SiO, and chlorine from NaCl (see the text).
[b] Asplund et al. (2009).

flows, respectively, with a radius of $\geqslant 900\ R_*$ at $f \sim 10^{-10}$. The distribution of HCO^+ mimics that of CO, except with a lower abundance profile. This result is consistent with the production of HCO^+ from protonation of carbon monoxide. The source distributions of SO, SO_2, and CS are similar for both outflows, except the red wind is more extended. The abundances of these three molecules reach a maximum closer to the star at $\sim 300\ R_*$, for both winds, and extend out to ~ 400 and $600\ R_*$ for the blue and red components, respectively. These results suggest that the chemistry of the three sulfur-bearing molecules is related, but the collimated outflows vary in their characteristics. Adande et al. (2013) and Singh et al. (2021) both suggested that SO and SO_2 were produced by shocks in such outflows.

4.3. Isotopic Ratios in NML Cyg

Table 5 lists sulfur, silicon, carbon, oxygen, and chlorine isotope ratios estimated from comparison of ESCAPADE abundances. The solar isotope ratios from Asplund et al. (2009) are also given in the table. For silicon, the ratios were derived from SiS, yielding $^{28}Si/^{29}Si = 33 \pm 10$, $^{28}Si/^{30}Si = 33 \pm 10$, and $^{29}Si/^{30}Si = 1.5 \pm 1.0$ for the spherical wind. These values agree with the solar ratios of 20, 30, and 1.5, respectively, within the uncertainties. (Asplund et al. 2009). In contrast, Andrews et al. (2022) found the following ratios for NML Cyg, based on SiO: $^{28}Si/^{29}Si \approx 10.9 \pm 0.9$, $^{28}Si/^{30}Si \approx 9.5 \pm 0.7$, and $^{29}Si/^{30}Si \approx 0.9 \pm 0.4$. However, these ratios were based solely on line intensities for SiO, which very likely has high opacities in the main isotopologue, resulting in artificially low numbers. For the O-rich AGB star IK Tauri, Velilla Prieto et al. (2017) found $^{28}Si/^{29}Si \sim 11–18$ and $^{28}Si/^{30}Si \sim 16–34$, based on SiO and SiS, and corrected for opacities. These values are comparable to those found in NML Cyg, although the comparison between hypergiant and AGB stars may not be completely valid. For NML Cyg, the survey suggests $^{32}S/^{34}S = 50 \pm 25$, as derived from SiS, also consistent with the solar value of 25, within the errors (see Table 4). Andrews et al. (2022) did not derive any sulfur isotope ratios, but values of $^{32}S/^{34}S \sim 10–15$ were estimated for the envelope of IK Tau (Velilla Prieto et al. 2017) and 32 in R Dor (Danilovich et al. 2016); both are O-rich AGB stars.

The carbon and oxygen isotope ratios are often problematic to calculate because of high opacities in the main isotopic lines typically used for these estimates. From HCN, the survey data indicate $^{12}C/^{13}C = 33 \pm 15$ in the spherical outflow. Milam et al. (2009) found a ratio of $^{12}C/^{13}C \sim 13$ for NML Cyg, based on a radiative transfer analysis of CO lines. These values are significantly lower than solar ratio of 89 and reflect the enhanced ^{13}C abundance produced from first and second dredge-up of the H-burning shell (see Milam et al. 2009; Ziurys et al. 2020). Based on HCN line intensities, Andrews et al. (2022) obtained $^{12}C/^{13}C \approx 9.3 \pm 1.5$. This lower value again likely results from high opacities in the main HCN line. From SiO, the survey suggests $^{16}O/^{18}O > 250$, while Andrews et al. obtained $^{16}O/^{18}O \approx 8.7 \pm 0.5$ from water lines. Again, high opacities are creating very low ratios in the latter case. Velilla Prieto et al. (2017) found a lower limit to the $^{16}O/^{18}O$ ratio of 60 for IK Tau, based on SiO.

Both chlorine isotopes, ^{35}Cl and ^{37}Cl, were detected in NaCl, with five transitions for the ground vibrational state observed per species, allowing for a reasonable evaluation of the $^{35}Cl/^{37}Cl$ ratio. For NML Cyg, we find $^{35}Cl/^{37}Cl = 3.9 \pm 0.3$. This value is very close in agreement with the solar ratio of 3.13 (Asplund et al. 2009). Cernicharo et al. (2000) reported a $^{35}Cl/^{37}Cl$ ratio of 3.1 ± 0.6 in the carbon-rich envelope of IRC+10216 from line intensity ratios of NaCl, KCl, and AlCl. The isotopes ^{35}Cl and ^{37}Cl are thought to be formed during both hydrostatic and explosive oxygen burning phases. The ^{35}Cl is created primarily through proton capture on ^{34}S; ^{37}Cl originates from the radioactive decay of ^{37}Ar, which also occurs during Ne burning (Woosley & Weaver 1995; Maas et al. 2016). Therefore, a solar-like ratio in both hypergiant and AGB stars for these isotopes is not unexpected, as they reflect the result of previous supernovae explosions and subsequent mixing.

5. Conclusions

The 1 mm survey of the hypergiant star NML Cyg is further evidence that objects of this type contain some of the most complex chemistry among the oxygen-rich envelopes. This result could arise from the unusual, episodic mass loss in these giant stars, marked by collimated outflows and shocked material. This work has also demonstrated that the envelope of NML Cyg closely resembles that of VY CMa, both in chemical content and in the presence of asymmetric winds, traced principally in sulfur-bearing molecules. The chemistry of NML Cyg, like VY CMa, is dominated by silicon- and sulfur-bearing species, but the carbon is not all contained in CO. Exotic species with sodium, aluminum, and phosphorus

are also present in this source. Finally, the Si, S, and Cl isotope ratios appear to be roughly solar with no particular anomalies. The $^{12}C/^{13}C$ ratio is low, as is expected at this stage of stellar evolution.

This research was supported by NSF grant AST- 1907910.

ORCID iDs

A. P. Singh https://orcid.org/0000-0002-5419-183X
L. M. Ziurys https://orcid.org/0000-0002-1805-3886

References

Adande, G. R., Edwards, J. L., & Ziurys, L. M. 2013, ApJ, 778, 22
Andrews, H., De Beck, E., & Hirvonen, P. 2022, MNRAS, 510, 383A
Asplund, M., Grevesse, N., Sauval, A. J., & Scott, P. 2009, ARA&A, 47, 481
Boboltz, D. A., & Claussen, M. J. 2004, ApJ, 608, 480
Cernicharo, J., Guelin, M., & Kahane, C. 2000, A&AS, 142, 181
Cohen, R. J., Downs, G., Emerson, R., et al. 1987, MNRAS, 225, 491
Danchi, W. C., Green, W. H., Hale, D. D. S., et al. 2001, ApJ, 555, 405
Danilovich, T., De Beck, E., Black, J. H., Olofsson, H., & Justtanont, K. 2016, A&A, 588, A119
Danilovich, T., Richards, A. M. S., Decin, L., Van de Sande, M., & Gottlieb, C. A. 2020, MNRAS, 494, 1323
Danilovich, T., Richards, A. M. S., Karakas, A. I., et al. 2019, MNRAS, 484, 494
Danilovich, T., Van de Sande, M., De Beck, E., et al. 2017, A&A, 606, A124
De Beck, E., Decin, L., Ramstedt, S., et al. 2017, A&A, 598, A53
Deguchi, S., & Goldsmith, P. F. 1985, Natur, 317, 336
Dubernet, M. L., Boudon, V., Culhane, J. L., et al. 2010, JQSRT, 111, 2151
Etoka, S., & Diamond, P. 2004, MNRAS, 348, 34
Herwig, F. 2000, A&A, 360, 952
Höfner, S., & Olofsson, H. 2018, A&AR, 26, 1
Humphreys, R. M., Davidson, K., Richards, A. M. S., et al. 2021, AJ, 161, 98
Humphreys, R. M., Helton, A. L., & Jones, T. J. 2007, AJ, 133, 2716
Humphreys, R. M., Ziurys, L. M., Bernal, J.J., et al. 2019, ApJL, 874, L26
Justtanont, K., Jong, T., de, Helmich, F. D., et al. 1996, A&A, 315, L217
Kamiński, T., Gottlieb, C. A., Menten, K. M., et al. 2013, A&A, 551, A113
Kaminski, T., Wong, K. T., & Schmidt, M. R. 2016, A&A, 592, A42
Kemper, F., Stark, R., Justtanont, K., et al. 2003, A&A, 407, 609
Maas, Z. G., Pilachowski, C. A., & Hinkle, K. 2016, AJ, 153, 196
Milam, S. N., Apponi, A. J., Woolf, N. J., & Ziurys, L. M. 2007, ApJ, 668, L131
Milam, S. N., Woolf, N. J., & Ziurys, L. M. 2009, ApJ, 690, 837
Monnier, J. D., Bester, M., Danchi, W. C., et al. 1997, ApJ, 481, 420
Müller, H. S. P., Schlöder, F., Stutzki, J., & Winnewisser, G. 2005, JMoSt, 742, 215
Nagayama, T., Koji, T., Toshihiro, O., et al. 2008, PASJ, 60, 1069
Nercessian, E., Guilloteau, S., Omont, A., & Benayoun, J. J. 1989, A&A, 210, 225
Netzer, N., & Knapp, G. R. 1987, ApJ, 323, 724
Olofsson, H. 2005, IAU Symp. 231, Astrochemistry: Recent Successes and Current Challenges, 1 ed. D. C. Lis, G. A. Blake, & E. Herbst (Cambridge: Cambridge Univ. Press), 499
Olofsson, H., Lindqvist, M., Winnberg, A., Nyman, L. Å. & Nguyen-Q-Rieu 1991, A&A, 245, 611
Omont, A., Lucas, R., Morris, M., & Guilloteau, S. 1993, A&A, 267, 490
Pickett, H. M., Poynter, R. L., Cohen, E. A., et al. 1998, JQSRT, 60, 883
Pulliam, R. L., Edwards, J. L., & Ziurys, L. M. 2011, ApJ, 743, 36
Quintana-Lacaci, G., Agúndez, M., Cernicharo, J., et al. 2016a, A&A, 592, A51
Richards, A. M. S., Yates, J. A., & Cohen, R. J. 1996, MNRAS, 282, 665
Saberi, M., Vlemmings, W. H. T., & De Beck, E. 2019, A&A, 625, A81
Schuster, M. T., Humphreys, R. M., & Marengo, M. 2006, AJ, 131, 603
Schuster, M. T., Marengo, M., Hora, J. L., et al. 2009, ApJ, 699, 1423
Singh, A. P., Edwards, J. L., Humphreys, R. M., & Ziurys, L. M. 2021, ApJL, 920, L38
Tenenbaum, E. D., Dodd, J. L., Milam, S. N., Woolf, N. J., & Ziurys, L. M. 2010a, ApJ, 720, L102
Tenenbaum, E. D., Dodd, J. L., Milam, S. N., Woolf, N. J., & Ziurys, L. M. 2010b, ApJS, 190, 348
Tenenbaum, E. D., Woolf, N. J., & Ziurys, L. M. 2007, ApJ, 666, L29
Tenenbaum, E. D., & Ziurys, L. M. 2009, ApJ, 694, L59
Tenenbaum, E. D., & Ziurys, L. M. 2010, ApJ, 712, L93
Tennyson, J., & Yurchenko, S. N. 2012, MNRAS, 425, 21
Teyssier, D., Quintana-Lacaci, G., Marston, A. P., et al. 2012, A&A, 545, A99
Velilla Prieto, L., Sánchez Contreras, C., Cernicharo, J., et al. 2017, A&A, 597, A25
Woods, P. M., Schöier, F. L., Nyman, L. Å., & Olofsson, H. 2003, A&A, 402, 617
Woosley, S. E., & Weaver, T. A. 1995, ApJS, 101, 181
Zhang, B., Reid, M. J., Menten, K. M., Zheng, X. W., & Brunthaler, A. 2012, A&A, 544, A42
Ziurys, L. M., Milam, S. N., Apponi, A. J., & Woolf, N. J. 2007, Natur, 447, 1094
Ziurys, L. M., Tenenbaum, E. D., Pulliam, R. L., Woolf, N. J., & Milam, S. N. 2009, ApJ, 695, 1604
Ziurys, L. M., Schmidt, D. R., & Bernal, J. J. 2018, ApJ, 856, 169
Ziurys, L. M., Schmidt, D. R., & Woolf, N. J. 2020, ApJL, 900, L31
Zubko, V., Li, D., Lim, T., Feuchtgruber, H., & Harwit, M. 2004, ApJ, 610, 427